Journal of Architectural and Planning Research
37:4 (Winter, 2023) 3

COMPOSITIONAL HETEROGENEITY OF HYBRID BINDER GELS IN AMBIENT-CURED FAYALITE-SLAG MORTARS: A MULTISCALE TERNARY REANALYSIS OF FE-RICH ALKALI-ACTIVATED SYSTEMS

Andrew Saint
Naveed Ahmad

Fe-rich fayalite slag (FS) is an attractive low-clinker precursor for alkali-activated construction materials, yet its ambient-temperature reactivity is intrinsically limited. A recent ambient-cured mortar study demonstrated that replacing 20 wt.% of FS with blast furnace slag (BFS) or ladle slag (LS) strongly improves kinetics, strength, ultrasonic pulse velocity, and resistance to water ingress. The present article interrogates the same three mortar systems — AAFS, AAFS-BFS, and AAFS-LS — through a different analytical lens focused on binder-gel heterogeneity rather than only average composition. The analysis integrates the reported experimental matrix, the published EDS ternary point clouds, the reported atomic ratios, and the accompanying phase and performance descriptors. Ternary point clouds from the reported EDS diagrams were reconstructed by a reproducible image-based digitization workflow, normalized in simplex-consistent coordinates, and quantified using centroid displacement, convex-hull area, and covariance-ellipse spread. The resulting compositional fields reveal distinctions that are not captured adequately by mean ratios alone. In the Ca-Al-Si plane, AAFS occupies a narrow Si-rich domain, whereas AAFS-BFS shifts toward a Ca-rich field and AAFS-LS exhibits the broadest Ca-Al-bearing distribution, with a hull area about 8.9 times that of AAFS. In the Na-Fe-Si plane, AAFS remains Fe-enriched with an elongated tail, AAFS-BFS concentrates in a compact Si-dominant field, and AAFS-LS occupies an intermediate Na-bearing domain. These compositional patterns align with the reported calorimetric acceleration, the emergence of C-(A)-S-H/C-(N)-A-S-H signatures alongside Fe-bearing gel participation, and the superior transport-related performance of the blended mortars. As a secondary analytical study based on published measurements, the field metrics are interpreted conservatively as robust descriptors of relative heterogeneity rather than as substitutes for raw point-wise EDS export.

https://doi.org/10.66033/japr2022-401

INTRODUCTION

The decarbonization of cement-based construction remains one of the central challenges in materials engineering because Portland cement production is both energy intensive and a major contributor to anthropogenic CO_2 emissions (Provis, 2018; Scrivener et al., 2018). Alkali-activated materials (AAMs) offer a route for valorizing industrial by-products as reactive precursors while simultaneously reducing clinker demand (Das et al., 2022; Provis, 2018). Among the more difficult precursor classes are Fe-rich non-ferrous slags, including fayalite slag (FS), which combine attractive waste-utilization potential with limited ambient-temperature reactivity (Komnitsas et al., 2020; Onisei et al., 2018). The chemical challenge is well established: FS is rich in Fe and Si but relatively poor in Ca and Al, so room-temperature alkali activation tends to form Fe-bearing sodium silicate gels with comparatively slow hardening and modest early strength (Adediran et al., 2021; Onisei et al., 2018; Peys et al., 2019).

A recent mortar study addressed this limitation by blending high-volume FS with 20 wt.% blast furnace slag (BFS) or ladle slag (LS) under ambient curing (Adediran et al., 2023). The work showed that both co-binders accelerated calorimetric response, shortened setting time, altered reaction products, improved workability, raised compressive strength, increased ultrasonic pulse velocity (UPV), and reduced water absorption and permeable porosity (Adediran et al., 2023). The same study also reported 100-point EDS ternary clouds and average atomic ratios for the binder gel, together with XRD, FTIR, TGA, and SEM observations. Those measurements are unusually rich because they connect chemistry, microstructure, and engineering properties within the same experimental framework.

However, the chemistry was interpreted mainly through average atomic ratios and qualitative ternary trends (Adediran et al., 2023). That leaves an important analytical gap. When hybrid alkali-activated gels are summarized by a single average composition, chemically distinct domains may be masked, especially in Fe-bearing systems where Ca-rich, Al-bearing, and Fe-rich reaction environments can coexist (Peys et al., 2019; Siakati et al., 2021; Siramanont et al., 2021). This issue is not merely semantic. The breadth, asymmetry, and displacement of a compositional field can influence nucleation pathways, interfacial transition zone (ITZ) development, pore refinement, and ultimately the balance among strength, transport resistance, and workability (Fang et al., 2021; San Nicolas & Provis, 2015). A field-based reinterpretation is therefore valuable even when the underlying measurements have already been reported, provided that the limits of figure-derived recovery are made explicit.

The objective of the present article is therefore to analyze the same ambient-cured FS mortar systems through a compositional-heterogeneity framework. Rather than asking only how the *mean* gel chemistry changes with BFS or LS, this study asks how the *shape* of the reported composition field changes, and whether those field-level changes help rationalize the reported differences in fresh and hardened properties. To do so, the published EDS ternary point clouds are reconstructed by image-based digitization, expressed in simplex-consistent coordinates, and integrated with the reported atomic ratios and performance metrics.

The article advances three connected hypotheses. First, the blended systems are better interpreted as broad hybrid compositional fields rather than as single average gels. Second, AAFS-LS and AAFS-BFS should diverge not only in mean chemistry but also in field breadth and directional bias, even though their average Ca/Si ratios are similar. Third, these field-level distinctions should align with the independently reported kinetic, microstructural, and transport-related differences. In that sense, the present study does not claim new experiments; instead, it contributes a more explicit,

reproducible, and field-aware interpretation of an already rich experimental dataset.

MATERIALS AND ANALYTICAL FRAMEWORK

Experimental context adopted in this study

The underlying mortar systems are the three ambient-cured formulations reported by Adediran et al. (2023): a fayalite-slag reference mortar (AAFS), an 80/20 FS-BFS blend (AAFS-BFS), and an 80/20 FS-LS blend (AAFS-LS). The original experimental program used the same activator chemistry across the three systems, with sodium hydroxide and sodium silicate mixed at a 1:1 mass ratio and cured at $23 \pm 2^{\circ}$C (Adediran et al., 2023). The source study also employed FS as both precursor and aggregate source, which is important because the microstructural interpretation already incorporates aggregate-binder interaction rather than paste chemistry alone (Adediran et al., 2021, 2023).

The present article uses the reported experimental context exactly as published for interpretation, including precursor chemistry, mineralogy, calorimetry, setting behavior, SEM-EDS, FTIR, TGA, XRD, compressive strength, UPV, water absorption, and permeable porosity (Adediran et al., 2023). The key matrix is summarized in Table 1. No new laboratory experiments are introduced here; the novelty lies in a geometry-aware reanalysis of the reported ternary EDS fields and their integration with the reported engineering results.

Table 1: Primary experimental context used in the present analysis, compiled from the reported mortar study (Adediran et al., 2023).

Sample	FS (wt.%)	BFS (wt.%)	LS (wt.%)	Core measurements available in the reported dataset
AAFS	100	0	0	Calorimetry, setting time, XRD, FTIR, TGA, SEM-EDS, workability, compressive strength, UPV, water absorption, permeable porosity
AAFS-BFS	80	20	0	Same measurement set under identical activator chemistry and ambient curing
AAFS-LS	80	0	20	Same measurement set under identical activator chemistry and ambient curing

The original activator had $SiO_2/Na_2O = 1.0$ and $H_2O/Na_2O = 15.7$, and the mortars were prepared using FS aggregate at an aggregate-to-precursor ratio of 3 (Adediran et al., 2023).

Image-derived compositional reconstruction

The core new dataset used in this article comes from the reported 100-point EDS ternary diagrams for the bulk binder gel of AAFS, AAFS-BFS, and AAFS-LS (Adediran et al., 2023). Because raw point tables were not publicly released with the article, the ternary clouds were reconstructed from the figure itself using image-based digitization. The PDF page containing the ternary diagrams was rendered at high resolution, the triangular boundaries were calibrated from the edge lines, and color-segmented point-support regions were recovered for the three reported clouds. Separate reconstructions were performed for the Ca-Al-Si and Na-Fe-Si ternary planes.

This approach was chosen deliberately. The goal was not to infer the exact original order of individual

EDS measurements, which would require access to the raw instrument export. Instead, the aim was to recover the geometry of the reported compositional fields — their centroids, directional shifts, spread, and outer envelopes — in a reproducible way. For field-geometry questions, the published point clouds already contain the relevant first-order information, even though they do not provide point-wise analytical precision.

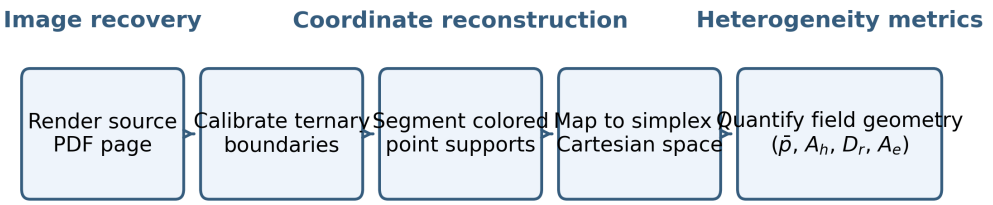

Figure 1: Reproducible workflow used to reconstruct and quantify the published ternary EDS point clouds from the reported figure. The procedure comprises page rendering, triangle calibration, color-based point isolation, simplex mapping, and field-geometry quantification.

To strengthen technical reliability, the triangle calibration was constrained by the visible edge intersections, the color segmentation was checked against the reported cloud locations and average-ratio trends, and all quantitative interpretation was limited to stable relative differences across the three systems. The digitized coordinate tables and figure-generation files used in this submission are provided with the manuscript package so that the reconstruction can be repeated directly.

Each ternary point support was normalized as a composition

$$\mathbf{x} = (x_1, x_2, x_3), \qquad x_j > 0, \qquad \sum_{j=1}^{3} x_j = 1, \tag{1}$$

which respects the simplex structure central to compositional data analysis (Aitchison, 1986; Egozcue et al., 2003). For visualization and area calculations, each ternary composition was mapped to Cartesian coordinates in an equilateral triangle,

$$\mathbf{p} = x_1 \begin{bmatrix} 1/2 \\ \sqrt{3}/2 \end{bmatrix} + x_2 \begin{bmatrix} 0 \\ 0 \end{bmatrix} + x_3 \begin{bmatrix} 1 \\ 0 \end{bmatrix}. \tag{2}$$

Geometric heterogeneity metrics

Three geometric measures were used to describe each reconstructed compositional field.

First, the centroid was computed as

$$\bar{\mathbf{p}} = \frac{1}{n} \sum_{i=1}^{n} \mathbf{p}_i, \tag{3}$$

which quantifies the directional displacement of the field within ternary space.

Second, the convex-hull area

$$A_h = \mathrm{area}\left(\mathrm{conv}\{\mathbf{p}_1, \ldots, \mathbf{p}_n\}\right) \tag{4}$$

was used as an outer-envelope measure of compositional breadth.

Third, two internal spread measures were computed: the mean radial deviation

$$D_r = \frac{1}{n}\sum_{i=1}^{n} \|\mathbf{p}_i - \bar{\mathbf{p}}\|_2 \tag{5}$$

and the covariance-ellipse proxy

$$A_e = 2\pi\sqrt{\det(\Sigma_{\mathbf{p}})}, \tag{6}$$

where $\Sigma_{\mathbf{p}}$ is the 2×2 covariance matrix of the Cartesian point cloud. Together, A_h, D_r, and A_e distinguish narrow, compact, anisotropic, and broad fields. In the present manuscript these descriptors are used as conservative, comparative summaries of field geometry; the ordering and separation among systems are emphasized more strongly than the exact absolute magnitude of any single metric.

The geometric interpretation was then cross-read with the reported average atomic ratios from the source article (Table 2), because a central question here is whether average ratios alone adequately describe the chemistry of the blended systems.

Performance integration

To relate compositional field geometry to macroscopic behavior, the geometric metrics were interpreted against the reported calorimetric, setting, mechanical, and transport indicators. The selected engineering descriptors were the cumulative heat release at 326 h, initial setting time, workability, 1-day strength, 28-day strength, early-age UPV, 28-day water absorption, and 28-day permeable porosity (Adediran et al., 2023). This multiscale integration is appropriate because the source study already linked higher reactivity and denser microstructure with improved performance, but did not quantify the internal compositional breadth of the gel field. The purpose here is therefore comparative rather than causal: the analysis tests whether independently reported performance trends are directionally consistent with the reconstructed field geometry.

Table 2: Reported average atomic ratios and selected engineering metrics used for multiscale interpretation (Adediran et al., 2023).

Sample	Ca/Si	Al/Si	Fe/Si	Na/Si	Heat[a]	Set[b]	Strength[c]	Absorp.[d]
AAFS	0.14	0.12	0.65	0.19	61	136	11	12
AAFS-BFS	0.65	0.15	0.23	0.13	70	50	32	9
AAFS-LS	0.66	0.43	0.64	0.76	75	30	34	6

[a] Cumulative heat release at 326 h, J/g.
[b] Initial setting time, min.
[c] 28-day compressive strength, MPa. The main text of the source article assigns 34 MPa to AAFS-LS and 32 MPa to AAFS-BFS; a reversed order appears in the concluding sentence. The values used here follow Section 3.7 of the source article.
[d] 28-day water absorption, %.

RESULTS

Mean compositional displacement is larger than average-ratio summaries imply

The reported average atomic ratios already indicate that the co-binders do more than simply add Ca to the system. Relative to AAFS, both blended systems show a large increase in Ca/Si, but they diverge sharply in Al/Si, Fe/Si, and Na/Si: AAFS-LS reaches Al/Si = 0.43 and Na/Si = 0.76, whereas AAFS-BFS remains much lower in both descriptors (Table 2). At the same time, AAFS and AAFS-LS retain similarly high Fe/Si ratios (0.65 and 0.64, respectively), while AAFS-BFS shifts to a much lower Fe/Si ratio of 0.23. These values already imply that the LS-modified system is not merely a stronger Ca source; it is chemically more hybrid.

The image-derived centroid analysis sharpens this picture, while still being read as a relative displacement map rather than as a substitute for raw point-wise EDS coordinates. In the Ca-Al-Si plane, the AAFS field remains strongly Si-dominant, with a centroid near $(\mathrm{Si}, \mathrm{Ca}, \mathrm{Al}) = (0.826, 0.087, 0.087)$. AAFS-BFS shifts the centroid toward a Ca-rich composition $(0.583, 0.320, 0.097)$, while AAFS-LS moves farther toward an Al-bearing field $(0.477, 0.311, 0.212)$. Thus, BFS and LS are both Ca-enriching additions, but only LS causes a substantial centroid shift toward Al-bearing compositions. This distinction is masked if the analysis stops at Ca/Si alone.

The Na-Fe-Si plane shows a second level of differentiation. AAFS is centered in an Fe-rich domain $(0.482, 0.114, 0.404)$ where Si and Fe jointly dominate the field. AAFS-BFS, by contrast, is centered in a Si-dominant composition $(0.741, 0.118, 0.141)$, indicating that BFS drives the gel field toward a more Si-rich, less Fe-dominated environment. AAFS-LS occupies an intermediate Na-bearing domain $(0.414, 0.334, 0.252)$, consistent with the much higher reported Na/Si ratio and with a more compositionally hybrid reaction product. These two ternary projections are shown in Figure 2.

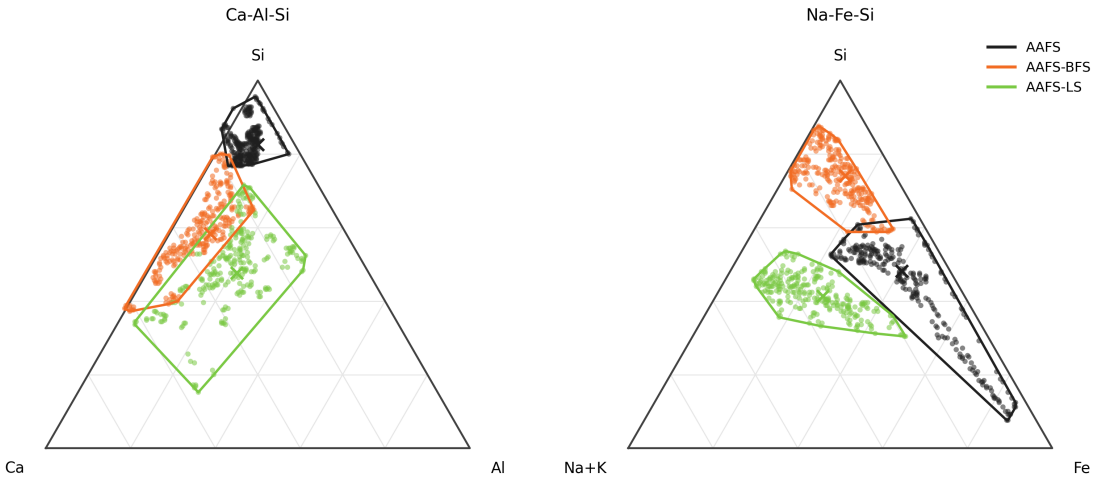

Figure 2: Digitized ternary fields reconstructed from the reported EDS diagrams for the bulk binder gel of AAFS, AAFS-BFS, and AAFS-LS. Transparent points represent image-derived point supports, solid outlines denote convex hulls, and cross-markers denote centroids. The figure is a new analysis product derived from the reported ternary diagrams in Adediran et al. (2023).

Compositional breadth reveals hidden differences between BFS and LS blends

The most important new result is that the blended systems differ not only in centroid position but also in field breadth. In the Ca-Al-Si plane, AAFS has the smallest convex-hull area ($A_h = 0.0117$) and the smallest internal spread ($D_r = 0.0363$), indicating a chemically constrained Si-rich field. AAFS-BFS expands that envelope substantially ($A_h = 0.0486$, $D_r = 0.0791$), while AAFS-LS produces the broadest field by a large margin ($A_h = 0.1046$, $D_r = 0.1053$). In other words, the LS blend creates a Ca-Al-Si compositional envelope roughly 8.9× wider than AAFS and just over 2× wider than AAFS-BFS.

The covariance-ellipse proxy leads to the same conclusion. In the Ca-Al-Si plane, A_e increases from 0.0047 for AAFS to 0.0181 for AAFS-BFS and to 0.0404 for AAFS-LS. Within the limits of figure-derived reconstruction, this is a clear indication that LS generates not just a shifted average composition, but a broader ensemble of local reaction environments. Such behavior is fully plausible given the LS mineralogy reported in the source study, which includes highly reactive mayenite and tricalcium aluminate phases in addition to a high bulk Al content (Adediran et al., 2023; Adesanya et al., 2017; Nguyen et al., 2019).

The Na-Fe-Si plane reveals a complementary pattern. AAFS exhibits the largest outer envelope in that plane ($A_h = 0.0706$), reflecting an elongated Fe-rich tail. This is consistent with the source article's identification of a dominant Fe-bearing sodium silicate character in AAFS and with the persistence of a weakly reacted, Fe-dominated matrix (Adediran et al., 2023; Onisei et al., 2018; Peys et al., 2019). AAFS-BFS is more compact in Na-Fe-Si space ($A_h = 0.0359$), which suggests a more chemically focused hybridization toward Si-rich Ca-bearing products. AAFS-LS has a slightly broader Na-Fe-Si envelope than AAFS-BFS ($A_h = 0.0414$), but still much less than AAFS. Taken together, the two ternary planes suggest that LS broadens the *Ca-Al-bearing* field more than it broadens the *Fe-bearing* field, while BFS narrows the Fe-rich signature most effectively.

Table 3: Image-derived compositional heterogeneity metrics for the reconstructed ternary fields.

Plane	Sample	Top	Left	Right	A_h	D_r	A_e
Ca-Al-Si	AAFS	0.826	0.087	0.087	0.0117	0.0363	0.0047
	AAFS-BFS	0.583	0.320	0.097	0.0486	0.0791	0.0181
	AAFS-LS	0.477	0.311	0.212	0.1046	0.1053	0.0404
Na-Fe-Si	AAFS	0.482	0.114	0.404	0.0706	0.0990	0.0297
	AAFS-BFS	0.741	0.118	0.141	0.0359	0.0758	0.0171
	AAFS-LS	0.414	0.334	0.252	0.0414	0.0847	0.0182

The "Top", "Left", and "Right" columns denote centroid coordinates in the corresponding ternary plane. A_h is convex-hull area, D_r is mean radial deviation, and A_e is the covariance-ellipse proxy defined in Section 2.3.

Compositional-field geometry aligns with kinetic and transport behavior

A useful test of the interpretation in Table 3 is whether it agrees with independent measurements. The agreement is directionally strong. The source article reported that cumulative heat release increased from 61 J/g for AAFS to 70 J/g for AAFS-BFS and 75 J/g for AAFS-LS, while the initial setting time shortened from 136 min to 50 min and 30 min, respectively (Adediran et al., 2023). Those changes are compatible with the compositional-field shifts documented here: both

blended systems depart strongly from the narrow Si-rich AAFS field, and AAFS-LS shows the widest Ca-Al-bearing field, consistent with the availability of reactive Ca- and Al-bearing phases.

The same correspondence appears at the level of engineering performance. The reported 28-day strength increases from 11 MPa for AAFS to 32–34 MPa for the blended mortars, while 28-day water absorption decreases from 12% to 9% (AAFS-BFS) and 6% (AAFS-LS) (Adediran et al., 2023). Figure 3 shows that the largest Ca-Al-Si field breadth occurs in AAFS-LS, the same system that combines the highest workability, the lowest absorption, and the lowest permeable porosity. Importantly, this distinction is not captured by Ca/Si alone because AAFS-BFS and AAFS-LS have nearly identical average Ca/Si values.

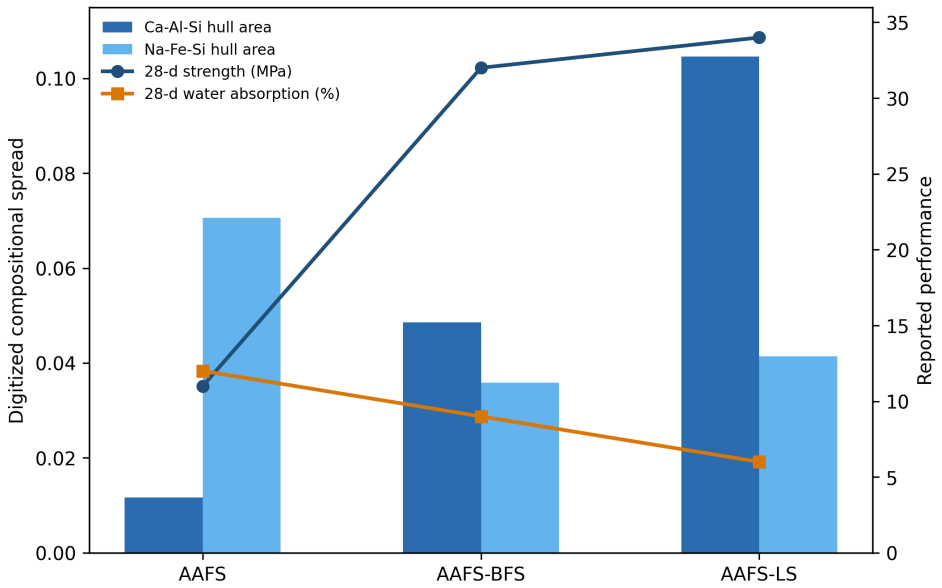

Figure 3: Relationship between image-derived compositional spread and selected reported 28-day performance indicators. The spread metrics are new analysis products; the strength and water-absorption values are reported in Adediran et al. (2023).

These results help rationalize why the LS blend outperforms the BFS blend in workability and transport resistance despite similar average Ca/Si values. The distinguishing feature is not simply *how much* Ca enters the gel field, but *how broadly* the field expands toward Ca-Al-bearing and Na-bearing domains while retaining Fe participation. That compositional breadth is consistent with the source article's XRD evidence of andradite formation, FTIR indications of C-(A)-S-H/C-(N)-A-S-H-like environments, TGA signatures of greater bound water, and SEM evidence of a denser ITZ in the blended mortars (Adediran et al., 2023; Fang et al., 2021; San Nicolas & Provis, 2015).

DISCUSSION

Why average chemistry is insufficient for hybrid Fe-rich AAMs

A key implication of the present study is that average-ratio reporting can obscure genuinely important chemistry in blended Fe-rich AAMs. If one compares only Ca/Si, AAFS-BFS and AAFS-LS appear nearly identical (0.65 and 0.66). Yet the reported performance is not identical, and the present field analysis shows why. AAFS-LS has a much larger Al-bearing shift, a much stronger Na-rich signature,

and a much broader Ca-Al-Si envelope. Hence, the two blends should not be interpreted as minor variants of the same gel chemistry. They are different compositional fields with different engineering consequences, even if the present study remains descriptive rather than point-wise mechanistic.

This conclusion is also consistent with the broader Fe-rich AAM literature. Studies on fayalite and CaO-FeO-SiO_2 slags have shown that Fe can remain an active part of the evolving binder rather than an inert residual phase (Onisei et al., 2018; Peys et al., 2019; Siakati et al., 2021). At the same time, Ca-bearing co-precursors promote C-(A)-S-H-like environments and hybrid gel features (Bernal et al., 2012; García-Lodeiro et al., 2008). The present results suggest that LS does not merely increase the amount of such hybridization; it broadens the admissible local chemistry across the material. That interpretation helps explain the combination of rapid hardening, high workability, and low water uptake reported for AAFS-LS, while remaining consistent with the limits of secondary analysis.

Implications for precursor pairing and ambient curing

The practical consequence is straightforward. In Fe-rich AAM design, co-binder screening should not end with bulk oxide chemistry or mean EDS ratios. Instead, co-binders should be evaluated according to the compositional fields they generate under the chosen activator and curing regime. The comparison here illustrates this clearly: BFS produces a strong and comparatively compact Si-rich hybrid field, which is favorable for strength development; LS, by contrast, creates a broader and more heterogeneous Ca-Al-bearing field, which appears especially beneficial for transport-related properties and fresh-state behavior. The practical message is therefore one of screening strategy: mean chemistry remains useful, but it should not be the only basis for co-binder selection in Fe-rich systems.

This perspective also helps rationalize ambient curing. Ambient-cured FS systems are fundamentally constrained by low intrinsic reactivity (Adediran et al., 2021; Komnitsas et al., 2020). The present analysis indicates that successful ambient blending is not only a matter of accelerating dissolution, but of opening chemically richer reaction-space trajectories that create denser and more functionally effective binder fields. In other words, ambient curing becomes viable when the precursor pairing engineers a favorable compositional field rather than only a favorable mean chemistry.

Limitations and reproducibility

The main limitation is that the compositional fields were reconstructed from published ternary diagrams rather than from raw EDS tables. Accordingly, the present metrics should be interpreted as geometric descriptors of the reported clouds, not as substitutes for the original instrument export. The approach nonetheless has two important strengths. First, it is reproducible from the published material and from the archived coordinate tables supplied with this submission. Second, the main conclusions are triangulated by independent observations already reported in the source study, including calorimetry, FTIR, XRD, TGA, SEM, strength, UPV, absorption, and porosity. For that reason, the analysis is best read as a validated secondary interpretation of relative field geometry, not as a replacement for primary microanalytical measurement.

A second limitation is that the present analysis does not assign exact phase fractions to specific gel families, nor does it prove causality between field geometry and performance. That would require raw point-wise EDS data, replicate-level uncertainty, and possibly combined spectroscopic or atomistic evidence. Even so, the compositional-field results are sufficiently distinct to support a

robust interpretive claim: the blended systems cannot be adequately described as single average gels, and AAFS-LS and AAFS-BFS differ in chemically meaningful ways despite similar Ca/Si averages.

CONCLUSIONS

This study examined the same ambient-cured FS mortar systems previously reported for AAFS, AAFS-BFS, and AAFS-LS, but through a compositional-heterogeneity framework centered on the geometry of the binder-gel ternary fields. Within the scope of the available evidence, the following conclusions can be drawn:

1. The binder-gel chemistry of the blended mortars is more informative when treated as a compositional field rather than a single average composition. Average Ca/Si alone is insufficient to differentiate BFS- and LS-modified systems.
2. In the Ca-Al-Si plane, AAFS remains a narrow Si-rich field, AAFS-BFS shifts toward a Ca-rich field, and AAFS-LS develops the broadest Ca-Al-bearing field. The LS blend exhibits a hull area approximately 8.9 times that of AAFS.
3. In the Na-Fe-Si plane, AAFS retains the strongest Fe-rich signature with an elongated tail, AAFS-BFS forms the most compact Si-dominant field, and AAFS-LS occupies an intermediate Na-bearing domain with persistent Fe participation.
4. The field-level distinctions align directionally with the independently reported kinetics, phase evolution, microstructure, and engineering performance. The broad Ca-Al-bearing field of AAFS-LS is consistent with its superior workability, lower water absorption, and lower permeable porosity.
5. For ambient-cured Fe-rich alkali-activated mortars, co-binder selection can be usefully framed as compositional field engineering. The decisive design question is not only how much Ca or Al is added, but how the co-binder reshapes the accessible reaction-space architecture of the binder gel.

ACKNOWLEDGMENT OF SOURCE DATASET

The ambient-cured mortar systems, performance metrics, and characterization outputs interpreted in this article were reported in the fayalite-slag mortar study by Adediran et al. (2023). The present manuscript contributes a new geometry-aware analysis of the reported EDS ternary fields and their relation to the reported multiscale measurements.

DATA AVAILABILITY

The image-derived digitization workflow, digitized coordinate tables, generated figures, and manuscript source files are provided with this submission package. The underlying experimental measurements are available from the original study authors on request, as stated in Adediran et al. (2023).

REFERENCES

Adediran, A., Yliniemi, J., & Illikainen, M. (2021). Development of sustainable alkali-activated mortars using Fe-rich fayalitic slag as the sole solid precursor. *Frontiers in Built Environment*, *7*, 653466. https://doi.org/10.3389/fbuil.2021.653466

Adediran, A., Yliniemi, J., Lemougna, P. N., Perumal, P., & Illikainen, M. (2023). Recycling high volume Fe-rich fayalite slag in blended alkali-activated materials: Effect of ladle and blast furnace slags on the fresh and hardened state properties. *Journal of Building Engineering*, *63*, 105436. https://doi.org/10.1016/j.jobe.2022.105436

Adesanya, E., Ohenoja, K., Kinnunen, P., & Illikainen, M. (2017). Alkali activation of ladle slag from steel-making process. *Journal of Sustainable Metallurgy*, *3*(2), 300–310. https://doi.org/10.1007/s40831-016-0089-x

Aitchison, J. (1986). *The statistical analysis of compositional data*. Chapman; Hall.

Bernal, S. A., Mejía de Gutiérrez, R., & Provis, J. L. (2012). Engineering and durability properties of concretes based on alkali-activated granulated blast furnace slag/metakaolin blends. *Construction and Building Materials*, *33*, 99–108. https://doi.org/10.1016/j.conbuildmat.2012.01.017

Das, S. K., Adediran, A., Kaze, C. R., Mustakim, S. M., & Leklou, N. (2022). Production, characteristics, and utilization of rice husk ash in alkali activated materials: An overview of fresh and hardened state properties. *Construction and Building Materials*, *345*, 128341. https://doi.org/10.1016/j.conbuildmat.2022.128341

Egozcue, J. J., Pawlowsky-Glahn, V., Mateu-Figueras, G., & Barceló-Vidal, C. (2003). Isometric logratio transformations for compositional data analysis. *Mathematical Geology*, *35*(3), 279–300. https://doi.org/10.1023/A:1023818214614

Fang, G., Wang, Q., & Zhang, M. (2021). Micromechanical analysis of interfacial transition zone in alkali-activated fly ash-slag concrete. *Cement and Concrete Composites*, *119*, 103990. https://doi.org/10.1016/j.cemconcomp.2021.103990

García-Lodeiro, I., Fernández-Jiménez, A., Blanco, M. T., & Palomo, A. (2008). FTIR study of the sol-gel synthesis of cementitious gels: C-S-H and N-A-S-H. *Journal of Sol-Gel Science and Technology*, *45*(1), 63–72. https://doi.org/10.1007/s10971-007-1643-6

Komnitsas, K., Yurramendi, L., Bartzas, G., Karmali, V., & Petrakis, E. (2020). Factors affecting co-valorization of fayalitic and ferronickel slags for the production of alkali activated materials. *Science of the Total Environment*, *721*, 137753. https://doi.org/10.1016/j.scitotenv.2020.137753

Nguyen, H., Adesanya, E., Ohenoja, K., Kriskova, L., Pontikes, Y., Kinnunen, P., & Illikainen, M. (2019). Byproduct-based ettringite binder – a synergy between ladle slag and gypsum. *Construction and Building Materials*, *197*, 143–151. https://doi.org/10.1016/j.conbuildmat.2018.11.165

Onisei, S., Douvalis, A. P., Malfliet, A., Peys, A., & Pontikes, Y. (2018). Inorganic polymers made of fayalite slag: On the microstructure and behavior of Fe. *Journal of the American Ceramic Society*, *101*(5), 2245–2257. https://doi.org/10.1111/jace.15420

Peys, A., White, C. E., Rahier, H., Blanpain, B., & Pontikes, Y. (2019). Alkali-activation of CaO-FeOx-SiO2 slag: Formation mechanism from in-situ X-ray total scattering. *Cement and Concrete Research*, *122*, 179–188. https://doi.org/10.1016/j.cemconres.2019.04.019

Provis, J. L. (2018). Alkali-activated materials. *Cement and Concrete Research*, *114*, 40–48. https://doi.org/10.1016/j.cemconres.2017.02.009

San Nicolas, R., & Provis, J. L. (2015). The interfacial transition zone in alkali-activated slag mortars. *Frontiers in Materials*, *2*, 70. https://doi.org/10.3389/fmats.2015.00070

Scrivener, K. L., John, V. M., & Gartner, E. M. (2018). Eco-efficient cements: Potential economically viable solutions for a low-CO_2 cement-based materials industry. *Cement and Concrete Research*, *114*, 2–26. https://doi.org/10.1016/j.cemconres.2018.03.015

Siakati, C., Douvalis, A. P., Hallet, V., Peys, A., & Pontikes, Y. (2021). Influence of CaO/FeO ratio on the formation mechanism and properties of alkali-activated Fe-rich slags. *Cement and Concrete Research*, *146*, 106466. https://doi.org/10.1016/j.cemconres.2021.106466

Siramanont, J., Walder, B. J., Emsley, L., & Bowen, P. (2021). Iron incorporation in synthetic precipitated calcium silicate hydrates. *Cement and Concrete Research*, *142*, 106365. https://doi.org/10.1016/j.cemconres.2021.106365

AUTOBIOGRAPHICAL SKETCHES

Andrew Saint, Department of Architecture, University of Cambridge

Naveed Ahmad, Norwegian University of Life Sciences

Manuscript revisions completed 09 September 2023.